Microscopic origin of magnetic anisotropy in martensitic Ni₂MnGa

P. Klaer, T. Eichhorn, G. Jakob, and H. J. Elmers

Institut für Physik, Johannes Gutenberg-Universität Mainz, D-55128 Mainz, Germany
(Received 23 March 2011; revised manuscript received 3 May 2011; published 15 June 2011)

The microscopic origin of magnetic anisotropy in the shape memory alloy Ni₂MnGa is investigated by means of x-ray magnetic circular dichroism in transmission mode. Field- and angle-dependent dichroism spectra of epitaxial Ni₂MnGa(101)/MgO(001) films reveal pronounced differences for magnetization aligned parallel and perpendicular to the film plane. These differences are related to an anisotropy of the orbital magnetic moment in agreement with the observed out-of-plane magnetocrystalline anisotropy. The spectral variation of the x-ray absorption originates from changes in the spin-projected density of states when the magnetization vector is rotated from the easy to the hard magnetic axis. Minority Ni states with $d_{3z^2-r^2}$ symmetry close to the Fermi energy form a wide half filled band for easy axis magnetization. When the magnetization is rotated into the hard axis the band narrowing of these states causes an increase of the mean kinetic energy of the electronic system. The opposite behavior of mostly unoccupied Ni states with d_{xy} symmetry leads to an increase of the minority orbital moment for hard-axis magnetization.

I. INTRODUCTION

Magnetic anisotropies essentially determine the hysteresis behavior of ferromagnets. The understanding of magnetic anisotropies in thin films is of crucial importance for the development of magnetic devices based on new materials.[1,2] While a huge amount of phenomenological data have been gathered, direct measurements of the origin of magnetic anisotropy, i.e., changes of the electronic states caused by the rotation of the magnetization vector with respect to the crystal lattice, remained scarce for itinerant ferromagnets.

An important class of materials where magnetic anisotropy is of utmost importance is provided by ferromagnetic shape memory alloys, which have attracted a great scientific and technological interest because they can show magnetic-field-induced strains of over 5% by the rearrangement of twin variants in the martensitic phase.[3,4] Many of these alloys are based on the Heusler alloy Ni₂MnGa and are potential smart materials for use in magnetomechanical actuators.[5] Epitaxial films are an important first step for the fabrication of microactuators based on free-standing films.[6–8] The driving force for the rearrangement of twin variants is delivered by the magnetic anisotropy energy.[9,10] Therefore an understanding of the electronic structure,[11] and in particular of the microscopic origin of the magnetic anisotropy,[12,13] is of great interest.

Models relating the magnetic crystal anisotropy to the atomic-orbital moment anisotropy have been successfully used to phenomenologically explain surface anisotropy[14–16] in ultrathin films. According to these models the orbital moment component parallel to the magnetization is partly suppressed when the magnetization vector is forced along the magnetic hard axis. Recently, however, orbital moment measurements on Au/Co/Au films showed a maximum value along the hard axis, in contrast with previous experience and indicating that the orbital moment anisotropy is not proportional to the magnetic anisotropy.[17] This observation was attributed to the large spin-orbit interaction within the Au at the interface. Another puzzling result of *ab initio* theory is the increase of the orbital moment for hard axis magnetization in Ni₂MnGa.[18]

Therefore a true bulk sensitive measurement of spin and orbital anisotropies, where interface effects can be neglected, is indispensable for establishing a thorough understanding of magnetic anisotropy.

Angular dependence of x-ray-absorption spectra has been used to investigate its correlation with structural distortions in oxides.[19] Atomic multiplet calculations reveal the strong effect of core hole interactions in this case. Here, we study metallic films with predominant itinerant electron states and the spectroscopic information obtained by x-ray magnetic circular dichroism (XMCD) reveals a distinct information on the electronic states that are relevant for the anisotropy energy.

The present paper provides experimental support for a simple model of magnetic anisotropy in Ni₂MnGa based on the anisotropy of atomic orbitals in a tetragonally distorted system in combination with spin-orbit coupling. Specific spectroscopic anisotropies in the XMCD spectra are related to maxima in the density-of-states function originating from high-symmetry points at the Brillouin-zone boundary.[20]

II. EXPERIMENT

We have grown Ni₂MnGa films with a typical thickness of 100 nm capped by 4 nm of Al by dc magnetron sputtering onto MgO(001) substrates at a substrate temperature of 650 °C.[21] Magnetic measurements were performed using a vibrating sample magnetometer (VSM). Temperature-dependent x-ray diffraction confirmed a martensitic phase transition at $T_m = 250$ K.[21,22]

X-ray-absorption spectroscopy (XAS) was performed at the UE56/1-SGM beamline at the German synchrotron light source BESSY II (Berlin) with the photon beam aligned with the external field of ±1.22 T if not otherwise stated. Spectra were measured at constant x-ray polarization switching the field at every energy step. The photon flux transmitted through the film was detected via x-ray luminescence in the substrate.[23,24]

III. EPITAXIAL STRUCTURE

Two circle x-ray diffraction in Bragg Brentano geometry reveals epitaxial growth of $Ni_2MnGa(101)$ films on MgO(001) [see Fig. 1(a)]. This naming convention sets the [0k0] direction parallel to the substrate surface. The orientation differs from the previously reported (001) orientation on MgO(001).[22] We suspect the high substrate temperature during deposition and small changes in the substrate surface due to formation of magnesium hydroxide prior to deposition to be responsible for this orientation observed in several samples. For substrates that were stored in vacuum or inert atmosphere prior to deposition we found (001) oriented growth exclusively. We have chosen films with (101) orientation for the present study because this orientation allows for a martensitic transformation with twin planes parallel to the surface [see Fig. 1(b)] thus largely avoiding elastic strain energy in the martensitic phase below $T_m = 250$ K, and a well defined uniaxial magnetic anisotropy.

The lattice constants in the cubic (martensitic) phase are $a_c = 0.581$ nm ($a_m = 0.607$ nm and $c_m = 0.551$ nm) resulting in the martensitic ratio $c/a = 0.91$. The values and directions of a_m and c_m have been measured at 120 K. Assuming volume conservation we get $b_m \approx a_c^3/(a_m c_m) \approx a_c$. Thus the martensite phase is in fact orthorhombic. The in-plane alignment of the film was probed by ϕ scans of the {022} and {004} reflections that enclose angles of 30° and 45° with the substrate surface, respectively.

For the (101) oriented films the ϕ scans reveal a multivariant growth with respect to the in-plane orientation. In a single crystal with the (101) plane aligned perpendicular to the ϕ axis, a ϕ scan of the {004} peaks would give two reflections, which correspond to the (004) and (400) reflection. This pair will differ by 180° in ϕ. In the {004} ϕ scan [Fig. 1(c)] obviously four variants, marked by different symbols, contribute. The sharp peaks between two {004} reflections are actually tails of the very strong {022} substrate reflections. This is evident by comparison to a ϕ scan of the {111} substrate reflections [Fig. 1(c)] being 45° rotated in plane.

The existence of four variants is confirmed by the ϕ scan of the {022} reflections [Fig. 1(c)]. The (022) Ni_2MnGa peak
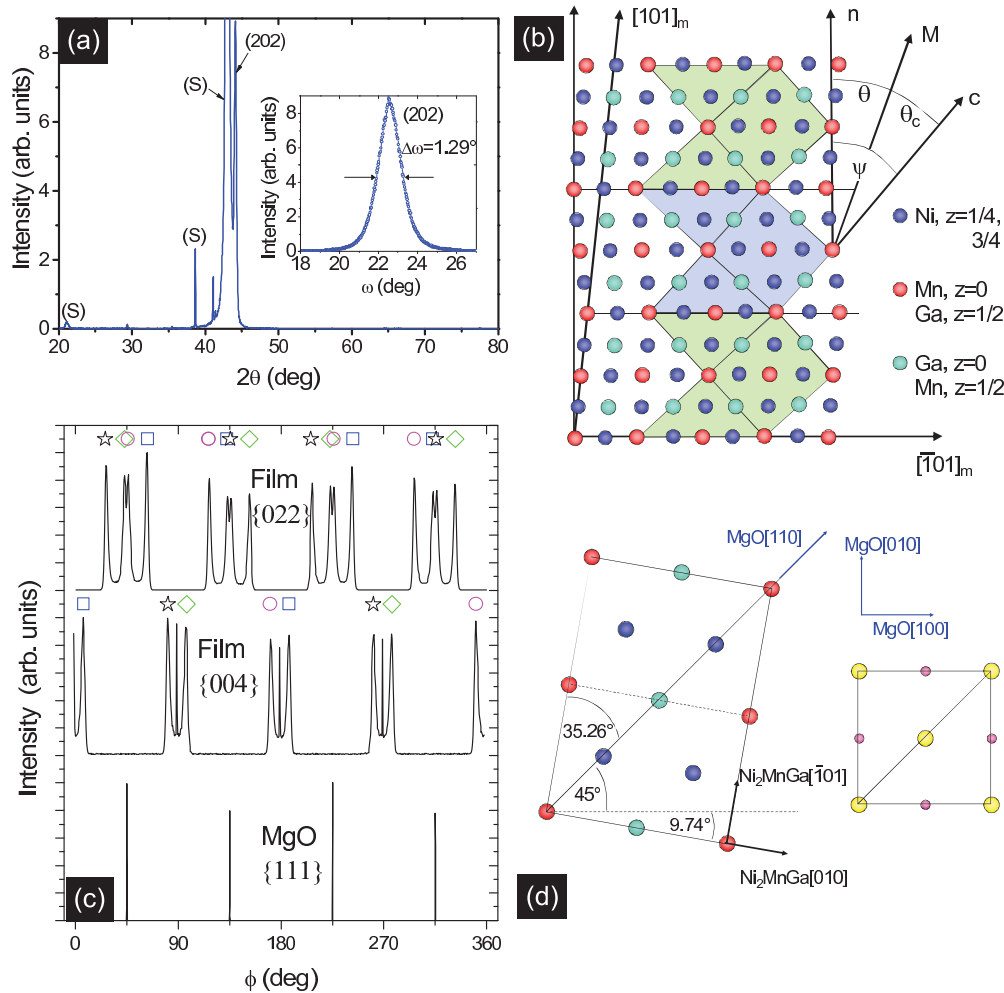

FIG. 1. (Color online) (a) Two circle x-ray diffraction in Bragg Brentano geometry of a $Ni_2MnGa(101)$/MgO(001) film. (b) Structural model of the martensitic phase neglecting modulation viewed along the Ni_2MnGa [010] axis. The position of the (101) twin planes is indicated by the horizontal lines. (c) Room-temperature ϕ scans of the {022} and {004} Ni_2MnGa film and MgO {111} reflections revealing four variants of the cubic phase indicated by different symbols. (d) Top view of the relative orientation of one of the four variants with respect to the substrate.

will appear at ϕ rotation of 54.74° with respect to the (004) peak of the same variant. In addition there will be a $(0\bar{2}2)$ peak in the opposite rotation direction and the corresponding (220) and $(2\bar{2}0)$ reflections. Thus the four variants will lead in total to 16 peaks in the ϕ scan of the {022} reflections. All these peaks are assigned to their respective variants by the symbols in Fig. 1(c).

The measured Ni$_2$MnGa [010] direction features a tilt of approximately $\pm 8°$ with respect to the [100] crystal axis of the substrate. This tilt can be motivated by inspection of the (101) plane of Ni$_2$MnGa. This plane has a rectangular symmetry as sketched in Fig. 1(d). A dense line of atoms is formed along the diagonal of the rectangle enclosing two surface unit cells [Fig. 1(d)]. The angle between the Ni$_2$MnGa [010] direction and this diagonal is calculated by $\arctan(2/\sqrt{2}) = 54.74°$. For the MgO(001) substrate surface the oxygen atoms form an fcc lattice in the plane and dense lines of oxygen atoms will form under $\pm 45°$. Assuming that the substrate-film interactions lead to a parallel orientation of dense lines one expects four variants with the [010] film direction showing 9.74° off from the MgO [100] and [010] direction in close agreement with the experimental observation.

Although the structure of the epitaxial film revealing already in the cubic phase four variants and eight variants in the martensitic phase appears complicated, the process of averaging upon measuring macroscopic physical properties results in a clear effective uniaxial symmetry: Averaging the two twin variants with their individual c axis oriented at an angle smaller than 45° with respect to the film normal results in a twofold symmetry within the {010} planes and an effective (short) c' axis along the surface normal n. This is explicitly calculated below for the case of magnetic anisotropy. In a similar way the four pairs of twin variants rotated azimuthally at $\pm 8°$ with respect to the in-plane MgO [100] and [010] axes lead to an effective fourfold symmetry comprising a considerably reduced in-plane anisotropy, which is neglected in the following. The remaining uniaxial anisotropy applies to the magnetic anisotropy, to the magnetic orbital moment and to the symmetry of the electronic structure as measured by x-ray absorption.

IV. MAGNETIC ANISOTROPY

The out-of-plane magnetic anisotropy was measured by hard-axis magnetization loops (see Fig. 2) exploiting the magneto-optical contrast of XMCD. We have tuned the photon energy to the Mn L_3 absorption edge providing the largest magnetic contrast. The x-ray-absorption signal was measured at constant circular polarization varying the external field applied perpendicular to the surface in steps of approximately 0.1 T. The value measured at zero external field was subtracted and the signal was normalized to the maximum value measured at maximum applied magnetic field.

The out-of-plane anisotropy energy $f(\theta) = L\cos^2\theta$ is a sum of shape anisotropy and crystal anisotropy according to $L = J_s^2/2\mu_0 + K_v$ with J_s being the saturation magnetization and K_v the bulk anisotropy constant. Interface anisotropies are neglected. Experimental results for the out-of-plane anisotropy constant are obtained from the saturation field H_s that is related to L by $H_s J_s = \partial^2 f(\pi/2)/\partial\theta^2 = 2L$. Defining the
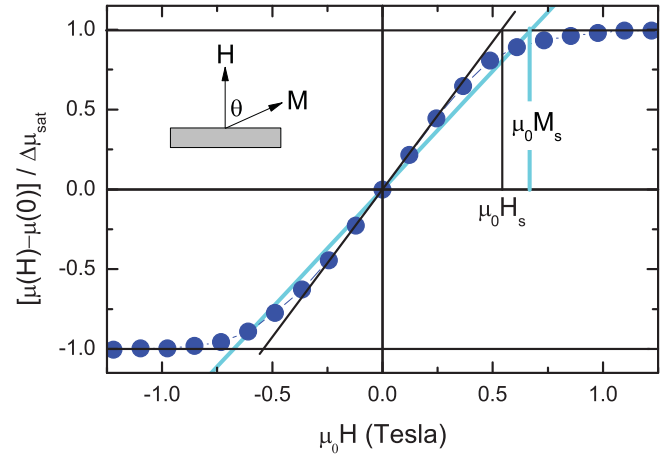

FIG. 2. (Color online) X-ray absorption $\mu(H)$ versus external field H applied perpendicular to the film surface (dots). The zero-field value $\mu(0)$ was subtracted and the difference was normalized to the saturation value $\Delta\mu_{sat}$ measured at the maximum field. The cross section of the initial susceptibility (black line) with the saturation value indicates the saturation field H_s. The initial susceptibility if only the shape anisotropy field $M_s = J_s/\mu_0$ were present is drawn for comparison [light-blue (gray) line].

anisotropy field $H_{anis} = 2K_v/J_s$, this results in the equation $H_s = J_s/\mu_0 + H_{anis}$ with the shape anisotropy field $M_s = J_s/\mu_0$. The saturation magnetization $J_s = 0.675$ T of the film was determined by a VSM magnetometer. The saturation field $\mu_0 H_s = 0.537$ T is determined from the hard-axis loop as shown in Fig. 2. Then we calculate the crystal anisotropy field $\mu_0 H_{anis} = \mu_0 H_s - J_s = -0.138$ T and an anisotropy constant of $K_v = H_{anis} J_s/2 = -3.7 \times 10^4$ J m^{-3}.

The negative sign indicates that the magnetic easy axis of the crystal anisotropy is perpendicular to the surface. Assuming that the anisotropy is exclusively caused by the Ni related states the anisotropy per atom e_{Ni} is calculated from the anisotropy constant K_v according to $e_{Ni} = K_v a_c^3/8 = -5.7 \ \mu$eV. We have used the volume of the unit cell as determined in the cubic phase by x-ray diffraction assuming that the value is not changed in the martensitic phase.

The magnetic anisotropy constant is in agreement with previously reported out-of-plane anisotropy constants for epitaxial Ni$_2$MnGa films[12,25] but an order of magnitude smaller than values reported for bulk single crystals.[26]

An explanation can be given as follows: The anisotropy in an individual twin variant can be described by

$$f_v(\theta',\phi') = K_c\cos^2\theta' + K_b\sin^2\theta'\sin^2\phi' \qquad (1)$$

with $\theta' = \theta_c$, ϕ' denoting the polar and azimuthal angle of the magnetization vector with respect to the c and a axis of the individual variant. The magnetization is homogeneous within the film because the magnetic exchange length is much larger than the length scale of the twin variant structure. Consequently, the variant structure [Figs. 1(b) and 1(d)] results in an averaged magnetic anisotropy. For averaging we first consider a rotation of the magnetization within the plane shown in Fig. 1(b) described by the polar angle θ between the film normal and the magnetization vector. In this case

we have $\phi' = 0$ and Eq. (1) simplifies to $f_v(\theta') = K_c \cos^2 \theta'$. The two twin variants tilted by $\pm\psi$ lead to the transformation $\theta' = \theta \pm \psi$ and after averaging one obtains for the free energy $f(\theta,\phi)$:

$$f(\theta,0) = K_c(\cos^2 \psi - \sin^2 \psi)\cos^2 \theta + K_c \sin^2 \psi. \quad (2)$$

The measured constant is thus reduced according to $K_{v,1} = K_c(\cos^2 \psi - \sin^2 \psi) = 0.083 K_c$ with the angle $\psi = \arctan(c/a)$ between the c axis and the film normal. Because the $[\bar{1}01]_m$ axis deviates by only a small angle from the MgO[010] axis along which the magnetization was rotated in the experiment, we neglect the azimuthal tilt and apply Eq. (2) to the set of two variants shown in Figs. 1(b) and 1(d) and to the corresponding two variants tilted by $-9.74°$. A further set of four variants exists which is rotated by the azimuthal angle of $90°$. Again we neglect the small azimuthal tilt. For perpendicular magnetization, $\theta = 0°$, the free energy is the same as in the case discussed before and one obtains $f(0,\pi/2) = f(0,0) = K_c \cos^2 \psi$. For in-plane magnetization the magnetization vector is directed parallel to the b axis, $[010]_m$, and one obtains $f(\pi/2,\pi/2) = f_v(\pi/2,\pi/2) = K_b$ according to Eq. (1). Thus the average anisotropy of this second set of variants is described by

$$f(\theta,0) = (K_c \cos^2 \psi - K_b)\cos^2 \theta + K_b. \quad (3)$$

Finally, the average of the two cases Eqs. (2) and (3) discussed above leads to

$$f(\theta,0) = \left[K_c(\cos^2 \psi - \tfrac{1}{2}\sin^2 \psi) - \tfrac{1}{2}K_b\right]\cos^2 \theta, \quad (4)$$

omitting terms independent on θ. This averaging step cancels the first-order in-plane anisotropy because an azimuthal rotation by $90°$ transforms the anisotropy of the first set of variants into the anisotropy of the second set and vice versa. Neglecting higher-order anisotropies a pure uniaxial anisotropy remains. Using the experimentally determined value for ψ we thus obtain $f(\theta,0) = (0.32 K_c - 0.5 K_b)\cos^2 \theta$. The relation between the experimentally measured anisotropy constant K_v and the single variant anisotropy constants is $K_v = 0.32 K_c - 0.5 K_b$.

K_c is supposed to be negative reflecting the easy axis along the c axis of a single variant. From the relation of the lattice constants $a > b > c$ with intermediate axis b one expects that K_b has an intermediate value according to $0 > K_b > K_c$. Let us assume that $K_b = K_c$. This is the case of two equal easy axes, i.e., equivalent to a tetragonal symmetry with one long and hard axis as discussed by theory.[5,18] This assumption then leads to an effective anisotropy constant of $K_v = -0.18 K_c$ with reversed sign in contradiction to the experimental result. We can thus exclude a tetragonal symmetry in our case. A sensible assumption is $K_b = 0.5 K_c$ taking into account that b is approximated by $b = (a + c)/2$. A similar relation for K_b was experimentally observed (see Ref. 10) and explained by a 14-M superstructure based on subunit cells with tetragonal symmetry. In this case we obtain $K_v = 0.07 K_c$, i.e., the measured anisotropy constant is an order of magnitude smaller than the anisotropy of an individual variant whereas the sign is conserved.

In summary, we find a crystal anisotropy with an easy axis pointing out of the film plane that is outbalanced by the shape anisotropy resulting in an easy-plane anisotropy of the film. The averaged crystal anisotropy is comparatively small but exhibits an order of magnitude larger values in a single twin variant. Assuming the relation $K_b = K_c/2$ for the anisotropy energies along the c and b axis with respect to the a axis of an individual twin variant one obtains a single variant anisotropy constant of $K_c = -0.53$ M J m^{-3} corresponding to a single atom anisotropy of $e_{c,\mathrm{Ni}} = -81\ \mu$eV, which is in agreement with previous observations.[10]

V. X-RAY-ABSORPTION SPECTROSCOPY

Figure 3 summarizes the XMCD results measured for different angles between x-ray beam/magnetization and surface normal. For $T > T_m$ no variations of the spectra were observed as expected for the cubic symmetry. Instead, in the martensitic state distinct changes in the XMCD spectra reveal the influence of the reduced crystal symmetry. Effective spin (including the magnetic dipole term) and orbital magnetic moments resulting from the sum-rule analysis[27,28] are plotted in Fig. 4.
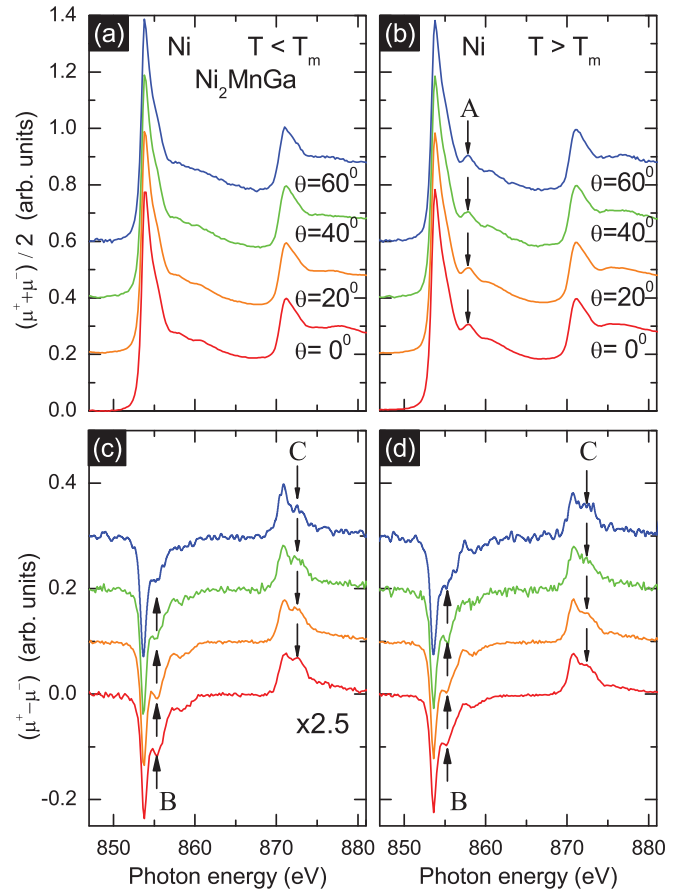

FIG. 3. (Color online) XAS (a,b) and corresponding XMCD (c,d) absorption coefficients calculated from the transmitted X-ray intensity measured at $T = 200$ K (a,c) and $T = 290$ K (b,d). The variation of the incidence angle between x-ray beam/magnetization and the surface normal is indicated in the figure. Peak A marks the satellite peak emerging in the austenitic state[22] and peaks B and C indicate angular dependent spectral changes caused by Ni d states with d_{xy} symmetry. Spectra and arrows are shifted with an identical offset for clarity.
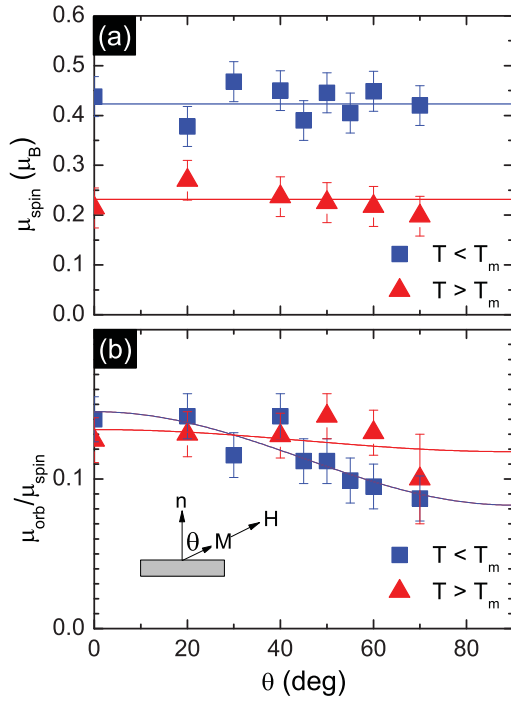
FIG. 4. (Color online) Angular dependence of the effective spin moment (a) and of the orbital to spin moment ratio (b) resulting from the sum-rule analysis at the Ni $L_{2,3}$ edge. The effective spin moment includes the magnetic dipole term. We assumed a number of d holes of $N_h = 1.5$ for Ni. Horizontal lines in (a) indicate the corresponding mean value of the effective spin moment. Full lines in (b) result from a fit to the function $\mu_{orb} = \mu_{orb}(0) - \Delta\mu_{orb}\sin^2\theta$.

FIG. 5. (Color online) (a) Site and spin-projected d-electron state densities for Ni (in arbitrary units) resulting from *ab initio* calculations (Ref. 29) shifted along the energy axis for direct comparison to the experimental data. Positive (negative) values indicate the majority (minority) density of states. (b) Difference of the XMCD signal measured at $\theta = 60°$ and normal incidence for $T < T_m$ [dark (blue) squares]. Full (red) line shows for comparison the XMCD signal measured at normal incidence.

For $T < T_m$ the orbital moment decreases with increasing angle between magnetization and surface normal. For $T > T_m$ no changes are observed. The spin moment is constant for both cases revealing a minor effect from the magnetic dipole anisotropy. Data at the Mn $L_{2,3}$ edge have also been measured and show no significant changes with incident angle above and below T_m. Thus the magnetic anisotropy is mainly caused by the Ni related electronic states.

We now compare the magnetic anisotropy determined above ($e_{Ni} = -5.7\ \mu eV$) with the anisotropy of the orbital magnetic moment $\Delta m_{orb} = 0.026\ \mu_B$. The negative sign of the crystal anisotropy is in qualitative agreement with the observed decrease in the orbital moment along the hard in-plane axis. A quantitative relation of the orbital moment variation Δm_{orb} and the magnetic anisotropy was discussed by Bruno:[16]

$$e_{Ni} = -C\frac{\xi}{4\mu_B}\Delta m_{orb}, \qquad (5)$$

where $\xi = 50$ meV is the spin-orbit coupling energy. The constant C depends on the band structure and is estimated to be smaller than $1/5$. Please note that the same reduction factor for variant averaging applies for e_{Ni} and Δm_{orb}. Using our experimental values of Δm_{orb} and e_{Ni} we calculate $C = 0.018$, which is roughly an order of magnitude smaller than expected. This can be viewed as an effect of the small exchange splitting relative to the bandwidth.

Spectroscopic changes in the Ni spectra with the magnetization angle [Fig. 5(b)] are emphasized by plotting the difference
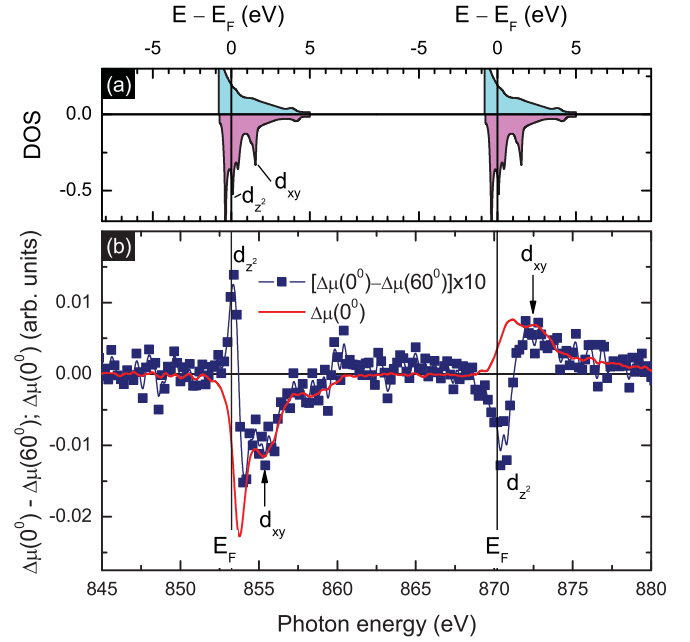
of the XMCD signal at normal incidence and at 60°. In a simple model we may interpret the difference as changes in the density of states (DOS) at the Ni site. This interpretation is further supported by the fact that data at the L_3 and L_2 edge are similar but with opposite sign, which would not be the case if multiplet effects were relevant. The opposite sign of the spectral shape observed at the L_3 and L_2 edge is a direct hint that the angular dependence is due to the spin asymmetry rather than to the orbital asymmetry.

Because the featureless majority DOS remains mostly unchanged upon magnetization rotation changes of the DOS are attributed to changes of the minority DOS. Hence the angular dependence of the XMCD probes the angular dependence of the minority DOS. Please note that the spin polarization of excited electrons is opposite at the L_3 and L_2 edge and in the usual notation the XMCD signal is negative at the L_3 edge. A positive difference [$\Delta\mu(0°) > \Delta\mu(60°)$] of XMCD values for $\theta = 0°$ and $\theta = 60°$ thus implies $|\Delta\mu(60°)| > |\Delta\mu(0°)|$, i.e., a stronger absolute XMCD signal for the in-plane orientation and thus also an enhanced DOS at the L_3 edge for the magnetic field aligned in-plane (vice versa for the L_2 edge).

The rotation of the magnetization affects the d states in a different way depending on the twin variant where the x-ray photon is absorbed. In our transmission experiment the measured signal results in an average over the eight twin variants. Similar to the case of the magnetic anisotropy this average leads to an effective uniaxial anisotropy of the electronic states, which is equivalent to a tetragonal structure with the short axis directing along the film normal.
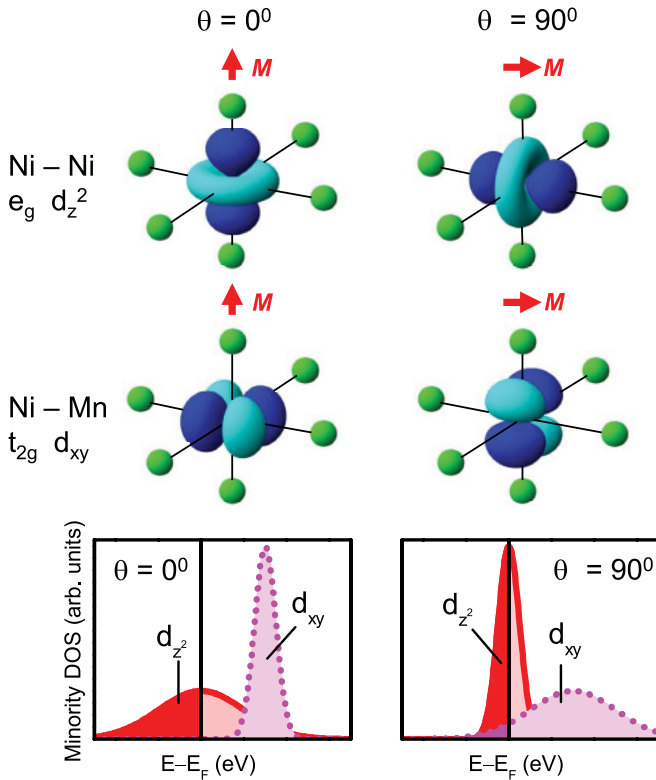
FIG. 6. (Color online) Sketch of the orbital symmetry of electron states with $d_{3z^2-r^2}$ (d_{z^2}) and d_{xy} symmetry indicating the dominating contribution to the DOS maxima for out-of-plane and in-plane magnetization direction, respectively. The two lower panels illustrate the opposite behavior of states with d_{z^2} and d_{xy} symmetry for perpendicular (left) and in-plane (right) magnetization. Dark shaded areas indicate occupied states.

A comparison with a calculation by Ayuela *et al.*[29] is shown in Fig. 5(a). The DOS is typically plotted versus energy where the Fermi energy is set to zero (see top axis). Electrons are excited by x-ray absorption from the $2p$ states of Ni (L_3 and L_2 edge), which are split by 16.9 eV due to the core shell spin-orbit coupling leading to two well separated absorption edges. The binding energies E_b of the $2p$ states are 853.2 and 870.1 eV. Thus a photon energy of $E_{ph} = h\nu$ excites electrons into unoccupied states above the Fermi energy at $E - E_F = E_{ph} - E_b$. In order to compare the XMCD signal with the calculated DOS the axis in Fig. 5(a) has been arranged in such a way that the energy scale is identical but shifted by the corresponding binding energy for both absorption edges.

The comparison to theory identifies the DOS maximum close to E_F with a $d_{3z^2-r^2}$ (d_{z^2}) state. The d_{z^2} state shows with its long axis parallel to the magnetization (see Fig. 6). With normal magnetization the nearest-neighbor atoms are close by because of the tetragonal distortion. Hence the hybridization is large, the bandwidth is also large, and the peak is small. If the magnetization is rotated along the in-plane direction, the d_{z^2} state hybridizes less with the neighboring atoms positioned at a larger distance. Accordingly, the bandwidth is smaller and the DOS d_{z^2} peak is larger. For the minority d_{xy} state at

1.5 eV above E_F the situation is opposite. For perpendicular magnetization the hybridization is small and the DOS peak is large. For in-plane magnetization the hybridization is larger and the DOS peak decreases.

The increased bandwidth of states with d_{z^2} symmetry in the case of $\theta = 0$ leads to a reallocation of occupied states (see Fig. 6) to lower kinetic energy because these states are nearly half filled. This reallocation thus decreases the total energy of the system thus explaining the occurrence of magnetic anisotropy with an easy axis along the perpendicular (short) axis. A state with d_{z^2} symmetry does not contribute to the orbital moment because its magnetic quantum number is zero.

On the other hand, the decreased bandwidth of states with d_{xy} symmetry for $\theta = 0$ reflects a decrease of corresponding states below E_F. This decrease counteracts the behavior of the d_{z^2} states discussed above but this effect is much smaller as the maximum is positioned at a higher energy. Because of the nonzero magnetic magnetic quantum number of the d_{xy} states the reduction of occupied states causes a reduction of the orbital magnetic moment. As the spin-orbit interaction favors parallel orbital and spin moments the reduction means a reduction of minority orbital moment, i.e., in fact, an increase of the total orbital moment in agreement with the experimental result.

VI. SUMMARY

In conclusion, we measured a change of the electron density of states in Ni$_2$MnGa upon rotation of the magnetization vector with respect to the crystal lattice. For this result we performed a model absorption experiment aligning the circular x-ray polarization and the magnetization with a large external field and varying the angle of incidence. By measuring in transmission mode any interface related effects are suppressed. The control experiment of the same sample in the cubic phase shows at least an order of magnitude smaller magnetic and spectral anisotropies. We illustrated that the bulk magnetocrystalline anisotropy in Ni$_2$MnGa is caused by a reallocation of electron states with $3d_{z^2}$ symmetry located predominantly at the Ni atom. On the other hand, the Ni orbital moment anisotropy is due to a a varying occupation of electron states with $3d_{xy}$ symmetry.

Our approach of a true bulk measurement of angular-dependent x-ray absorption for epitaxial films provides access to both magnetic and electronic anisotropies. The measurement of the DOS for different magnetization directions in metals provides an alternative pathway to understand spin-orbit coupling and magnetic anisotropy in materials with itinerant electron states.

[1] U. Gradmann, in *Handbook of Magnetic Materials*, edited by K. H. J. Buschow(Elsevier, Amsterdam, 1993), p. 1.

[2] C. A. F. Vaz, J. A. C. Bland, and G. Lauhoff, Rep. Prog. Phys. **71**, 056501 (2008).

[3] K. Ullakko, J. K. Haung, C. Kanter, V. V. Korkorin, and R. C. O'Handley, Appl. Phys. Lett. **69**, 1966 (1996).

[4] K. Otsuka and C. M. Wayman, *Shape Memory Materials* (Cambridge University Press, Cambridge, England, 1998).

[5] P. Entel, V. D. Buchelnikov, V. V. Khovailo, A. T. Zayak, W. A. Adeagbo, M. E. Gruner, H. C. Herper, and E. F. Wassermann, J. Phys. D **39**, 865 (2006).

[6] P. Pörsch, M. Kallmayer, T. Eichhorn, G. Jakob, H. J. Elmers, C. A. Jenkins, C. Felser, R. Ramesh, and M. Huth, Appl. Phys. Lett. **93**, 022501 (2008).

[7] O. Heczko, M. Thomas, J. Buschbeck, L. Schultz, and S. Fähler, Appl. Phys. Lett. **92**, 072502 (2008).

[8] M. Thomas, O. Heczko, J. Buschbeck, Y. W. Lai, J. McCord, S. Kaufmann, L. Schultz, and S. Fähler, Adv. Mater. **21**, 3708 (2009).

[9] J. Enkovaara, A. Ayuela, L. Nordstrom, and R. M. Nieminen, Phys. Rev. B **65**, 134422 (2002).

[10] S. Kaufmann, U. K. Rössler, O. Heczko, M. Wuttig, J. Buschbeck, L. Schultz, and S. Fähler, Phys. Rev. Lett. **104**, 145702 (2010).

[11] C. P. Opeil, B. Mihaila, R. K. Schulze, L. Manosa, A. Planes, W. L. Hults, R. A. Fisher, P. S. Riseborough, P. B. Littlewood, J. L. Smith, and J. C. Lashley, Phys. Rev. Lett. **100**, 165703 (2008).

[12] V. A. Chernenko, V. Golub, J. M. Barandiaran, Y. Salyuk, F. Albertini, L. Righi, S. Fabbrici, and M. Ohtsuka, Appl. Phys. Lett. **96**, 042502 (2010).

[13] M. A. Uijttewaal, T. Hickel, J. Neugebauer, M. E. Gruner, and P. Entel, Phys. Rev. Lett. **102**, 035702 (2009).

[14] D. Weller, J. Stohr, R. Nakajima, A. Carl, M. G. Samant, C. Chappert, R. Megy, P. Beauvillain, P. Veillet, and G. A. Held, Phys. Rev. Lett. **75**, 3752 (1995).

[15] H. A. Dürr, G. Y. Guo, G. van der Laan, J. Lee, G. Lauhoff, and J. A. C. Bland, Science **277**, 5323 (1997).

[16] P. Bruno, Phys. Rev. B **39**, 865 (1989).

[17] C. Andersson, B. Sanyal, O. Eriksson, L. Nordstrom, O. Karis, D. Arvanitis, T. Konishi, E. Holub-Krappe, and J. H. Dunn, Phys. Rev. Lett. **99**, 177207 (2007).

[18] M. E. Gruner, P. Entel, I. Opahle, and M. Richter, J. Mater. Sci. **43**, 3825 (2008).

[19] G. van der Laan, R. V. Chopdekar, Y. Suzuki, and E. Arenholz, Phys. Rev. Lett. **105**, 067405 (2010).

[20] J. Stohr, J. Magn. Magn. Mater. **200**, 470 (1999).

[21] G. Jakob and H. J. Elmers, J. Magn. Magn. Mater. **310**, 2779 (2007).

[22] G. Jakob, T. Eichhorn, M. Kallmayer, and H. J. Elmers, Phys. Rev. B **76**, 174407 (2007).

[23] M. Kallmayer, H. Schneider, G. Jakob, H. J. Elmers, K. Kroth, H. Kandpal, U. Stumm, and C. Cramm, Appl. Phys. Lett. **88**, 072506 (2006).

[24] M. Kallmayer, H. Schneider, G. Jakob, H. J. Elmers, B. Balke, and S. Cramm, J. Phys. D **40**, 1552 (2007).

[25] V. Golub, K. M. Reddy, V. Chernenko, P. Müllner, A. Punnoose, and M. Ohtsuka, J. Appl. Phys. **105**, 07A942 (2009).

[26] R. C. O'Handley and S. M. Allen, in *Encyclopedia of Smart Materials*, edited by M. Schwartz (Wiley, New York, 2002).

[27] B. T. Thole, P. Carra, F. Sette, and G. van der Laan, Phys. Rev. Lett. **68**, 1943 (1992).

[28] P. Carra, B. T. Thole, M. Altarelli, and X. Wang, Phys. Rev. Lett. **70**, 694 (1993).

[29] A. Ayuela, J. Enkovaara, and R. M. Nieminen, J. Phys.: Condens. Matter **14**, 5325 (2002).